# Charge carrier density, mobility, and Seebeck coefficient of melt-grown bulk $ZnGa_2O_4$ single crystals

Cite as: AIP Advances 10, 055005 (2020); doi: 10.1063/5.0002847
Submitted: 28 January 2020 • Accepted: 9 April 2020 •
Published Online: 5 May 2020



Johannes Boy,[1,a)] Martin Handwerg,[1] Rüdiger Mitdank,[1] Zbigniew Galazka,[2] and Saskia F. Fischer[1,b)]

## AFFILIATIONS

[1] Novel Materials Group, Humboldt-Universität zu Berlin, Newtonstraße 15, 12489 Berlin, Germany
[2] Leibniz-Institut für Kristallzüchtung, Max-Born-Strasse 2, 12489 Berlin, Germany

[a)] **Author to whom correspondence should be addressed:** boy@physik.hu-berlin.de
[b)] sfischer@physik.hu-berlin.de

## ABSTRACT

The temperature dependence of the charge carrier density, mobility, and Seebeck coefficient of melt-grown, bulk $ZnGa_2O_4$ single crystals was measured between 10 K and 310 K. The electrical conductivity at room temperature is about $\sigma = 286$ S/cm due to a high electron concentration of $n = 3.26 \times 10^{19}$ cm$^{-3}$ caused by unintentional doping. The mobility at room temperature is $\mu = 55$ cm$^2$/V s, whereas the scattering on ionized impurities limits the mobility to $\mu = 62$ cm$^2$/Vs for temperatures lower than 180 K. The Seebeck coefficient relative to aluminum at room temperature is $S_{ZnGa_2O_4-Al} = (-125 \pm 2)\ \mu$V/K and shows a temperature dependence as expected for degenerate semiconductors. At low temperatures, around 60 K, we observed the maximum Seebeck coefficient due to the phonon drag effect.



## I. INTRODUCTION

Transparent conducting oxides (TCOs) have drawn attention due to their possible application in high-power, optical, or gas sensing devices.[1–8] Recently, $\beta$-$Ga_2O_3$ and related semiconducting oxides with ultra-wide bandgaps of over 4 eV are in the focus, since they offer transparency in the visible spectrum, semiconducting behavior, and breakthrough electric fields of several MV/cm. The fundamental research has been extended from binary to ternary and quaternary systems to find new substrate material for epitaxial thin film growth, as well as to make use of a higher degree of freedom in terms of doping.[9]

$ZnGa_2O_4$ is a novel ternary conducting oxide that crystallizes in the spinel crystal structure, which makes it interesting as a substrate for ferrite spinels.[9] Furthermore, the material might be promising for electrical application, which gives rise to a study of the fundamental electric and thermoelectric transport properties. The isotropic thermal conductivity at room temperature is $\lambda = 22$ W/mK,[9] but many other material parameters remain to be clarified. Theoretical values for the bandgap of $ZnGa_2O_4$ were predicted to be indirect (K-Γ) with values between 2.69 eV–4.71 eV[10–16] or direct (Γ-Γ) with a value of 2.79 eV.[17] The experimental bandgap was found at values of 4.0–5.0 eV measured on synthetized ZnO:$Ga_2O_3$ powders,[18] ceramics,[19] films obtained by mist-CVD,[20] films obtained by sol–gel,[21] and bulk crystals obtained by the flux method,[22] while the experimental optical bandgap measured on bulk single crystals obtained from the melt is 4.6 eV.[9] Theoretically calculated effective masses are in the range of $m^* = 0.22$–$0.66\ m_e$.[13,15–17] Little is known about electric transport parameters. On the one hand, $ZnGa_2O_4$ ceramics show low electrical conductivity ($\sigma_{ZnGa_2O_4,ceram.} \approx 30$ S/cm[19]). On the other hand, melt-grown bulk single crystals showed a high electrical conductivity of about 50–500 S/cm.[9]

In this work, we investigate as-grown bulk $ZnGa_2O_4$ of blueish coloration and perform temperature-dependent Seebeck, van der Pauw, and Hall measurements between $T = 10$ K and $T = 310$ K. We discuss the results in terms of electron scattering processes and thermoelectric effects observed using a degenerate semiconductor.

The samples have been grown using the vertical gradient freeze method,[9] without intentional doping. Powdered ZnO and $Ga_2O_3$, each with a purity of 99.999%, were used as starting materials. The growth was performed in an Ir crucible with an excess of 0.2 mol. % of ZnO to compensate its losses at high temperatures. The growth atmosphere consisted of $O_2$/Ar (20 vol. %/80 vol. %). The heating up and cooling down times were 7 h and 10 h, respectively, and resulted in single crystal blocks with a blue and transparent appearance. As can be seen from Ref. 9 (Fig. 7), the composition of the obtained crystals was close to stoichiometric. All crystals grown in this way showed a similar defect structure as has been reported,[9] without low-angle grain boundaries. For further details on the growth conditions and structural and chemical characterization of the material, see the study by Galazka *et al.*[9]

## II. EXPERIMENTAL DETAILS

To perform electric and thermoelectric measurements, a microlab, consisting of metal lines, has been manufactured on the surface. Figure 1 shows a microscopic image and a schematic view of the microlab, which allows the measurement of the Seebeck coefficient, conductivity using the van der Pauw method, and the Hall resistance. The Ohmic contacts used for measuring the thermovoltage $U_{th}$ are located in the middle of the four-point metal lines (Ohmic contacts 1 and 3 in Fig. 1), which serve as thermometers and allow the measurement of the temperature difference $\Delta T$.

The microlab has been manufactured by standard photolithography and magnetron sputtering of titanium (7 nm) and gold (35 nm), after cleaning with acetone and isopropanol and subsequent drying. The as-sputtered metal lines of the microlab are isolated due to a Schottky contact relative to the $ZnGa_2O_4$ bulk crystal. Ohmic contacts with the $ZnGa_2O_4$ bulk crystal were achieved by direct wedge bonding with an Al/Si-wire (99%/1%) on the

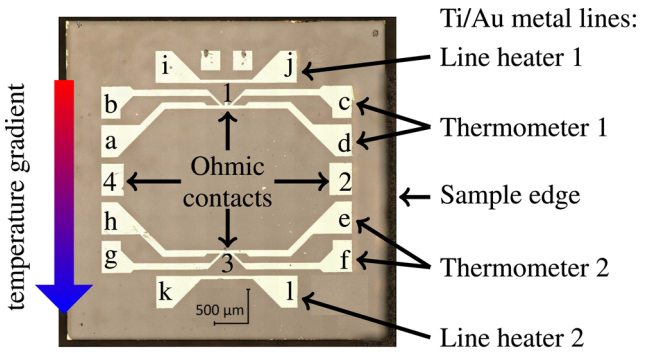


**FIG. 1.** Overview of the function of the Seebeck microlab consisting of Ti/Au lines. A two-point conductor at the top (or bottom) of the picture serves as a line heater (*Line heater* 1) to create a temperature gradient $\Delta T$ across the sample. Line heater 2 at the bottom may be used in case Line heater 1 gets damaged. The temperature difference is being measured by the change in the four-point resistance in the thermometer lines at the bottom of the sketch (*Thermometer* 2) and below the line heater (*Thermometer* 1). At marks 1 and 3, Ohmic contacts were prepared, which are used to measure the thermovoltage ($U_{th}$). Additional Ohmic contacts (2 and 4) are located at the sample edges and allow van der Pauw measurements. The two unlabeled pads above Line heater 1 were used in advance for technical investigations and do not affect this study. See text for further details.

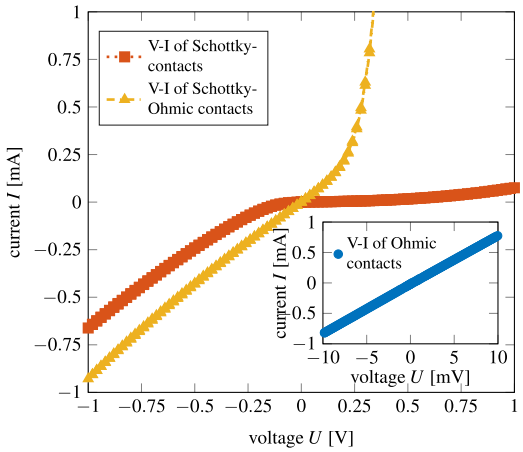


**FIG. 2.** Exemplary two-point *I–V* curves at room temperature between two Ohmic contacts (contacts 1 and 2 in Fig. 1) achieved by wedge-bonding with aluminum wire (inset) with a resistance of $R_{ohm.} \approx 12\ \Omega$ and two separated heater lines manufactured by standard photolithography and magnetron sputtering of Ti/Au (7 nm/35 nm) which are in contact with Au wire and Indium (red squares, contacts i and k in Fig. 1) and a Schottky diode contact (yellow triangles, contacts 1 and i in Fig. 1). The dynamic resistance of the Schottky barriers in reverse bias is at least two orders of magnitude higher, $R_{dyn.,sch} \geq 1000\ \Omega$, than that of the Ohmic contact.

deposited metal structure, creating point contacts. To keep some parts of the microlab isolated relative to the thin film, electrical contacts were prepared by attaching a gold wire with indium to the Ti/Au metal lines (at positions a–l in Fig. 1). This procedure can be compared to the one used with $\beta$-$Ga_2O_3$, shown in Refs. 23 and 24. Figure 2 displays exemplary two-point I–V curves at room temperature.

The experimental procedure is carried out in a CryoVac Konti-IT flow cryostat between $T = 10$ K and $T = 320$ K. The sample is in a helium atmosphere at standard pressure. After the bath temperature is stabilized, the van der Pauw and Hall measurements are carried out. Subsequently, the Seebeck measurements are performed. The Seebeck measurements involve the creation of various temperature differences by imprinting different currents into the line heater. The thermovoltage is measured simultaneously for approximately 3 min, which allows us to create a stable temperature difference across the sample. Then, while keeping the heating current constant, the resistances of the thermometers are measured. This procedure is repeated within bath temperature intervals of 10 K.

## III. MEASUREMENT RESULTS

We present the measurement results of the electric and the thermoelectric transport, as shown in Figs. 2–8. To quantify the quality of the contacts, two-point *I–V* curves were measured at room temperature and are shown in Fig. 2. The red square and orange triangles in the main plot show the *I–V* curves of Schottky–Schottky (contacts i and k in Fig. 1) and Schottky–Ohmic contacts (contacts 1 and i in Fig. 1), respectively. The *I–V* curve for the Ohmic–Ohmic contact configuration (contacts 1 and 2 in Fig. 1) can be seen as blue circles in the inset. The two-point *I–V* graphs of the different Schottky contact configurations show the expected diode curve for

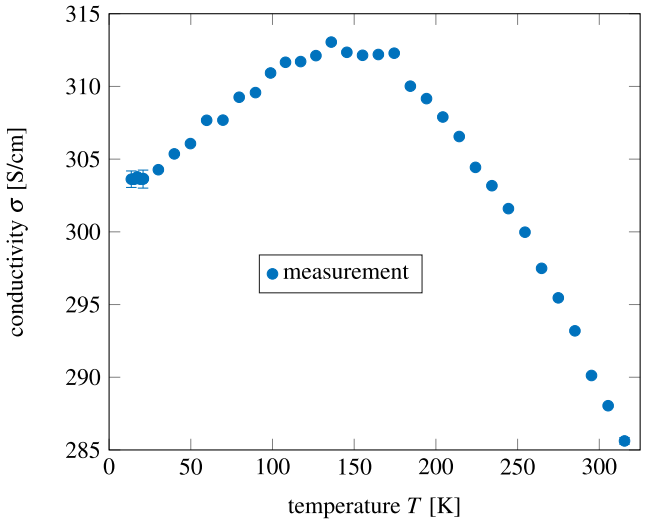


**FIG. 3**. Conductivity $\sigma$ as a function of temperature $T$. The conductivity reaches a maximum in the temperature range of $T$ = 125 K to $T$ = 175 K and shows a rather weak temperature dependence.

forward bias (positive voltages) as well as reverse bias (negative voltages). The dynamic resistance of the Schottky–Ohmic and Schottky–Schottky contacts is at least two orders of magnitude higher than the Ohmic–Ohmic contact resistance of 12 Ω, shown in the inset. Therefore, a good electrical isolation between the heater lines and the $ZnGa_2O_4$ bulk crystal is achieved.

The temperature dependence of the electrical conductivity $\sigma$ is shown in Fig. 3. The conductivity is between 285 and 315 S/cm for

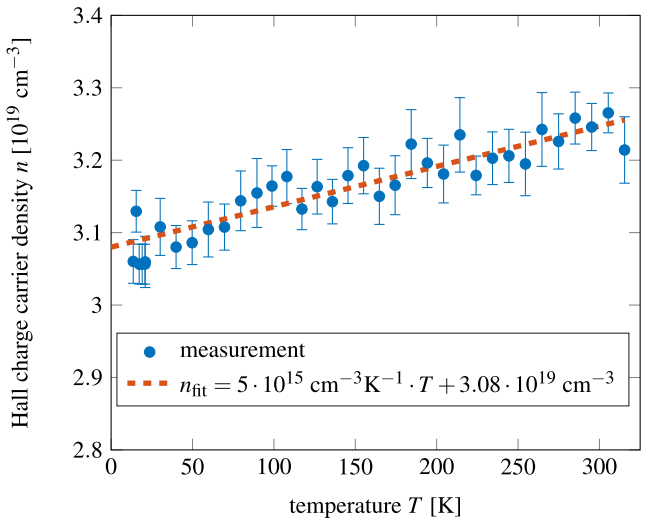


**FIG. 4**. Hall charge carrier density $n$ as a function of temperature $T$. A simple linear fit model has been applied to the data (red dashed line). It can be seen that the overall change in charge carrier density in the temperature range of $T$ = 10 K to $T$ = 320 K is more than one order of magnitude smaller than the Hall charge carrier density.

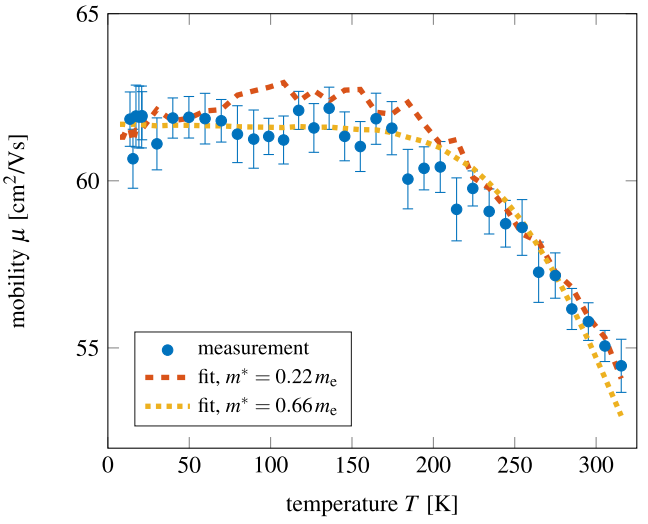


**FIG. 5**. Mobility $\mu$ as a function of temperature $T$. Two fits for $m^*$ = 0.22$m_e$ (red dashed line) and $m^*$ = 0.66$m_e$ (yellow dotted line) have been calculated with Eqs. (6)–(10) and plotted. The high temperature dependence can be explained by electron scattering with polar optical phonons. One can observe saturation of the mobility for temperatures lower than $T \leq$ 180 K. This can be explained by electron scattering with ionized impurities.

the entire temperature range. For higher temperatures, $T \geq$ 260 K, the conductivity $\sigma$ is decreasing. A maximum can be identified around $T$ = 150 K.

Hall measurements were performed to determine the charge carrier density, which is depicted as a function of temperature in Fig. 4. A linear fit has been added to the plot, showing weak temperature dependence. The Hall charge carrier density is at $n$ = 3.1 × $10^{19}$ $cm^{-3}$ for the entire temperature range.

The measurement of electrical conductivity and Hall charge carrier density allows the calculation of the electron mobility $\mu$. The electron mobility as a function of temperature is plotted in Fig. 5. At room temperature, a mobility of $\mu$ = 55 $cm^2$/V s was measured. The mobility increases with a decrease in temperature until it reaches a plateau-like feature of $\mu$ = 62 $cm^2$/V s at $T$ = 180 K and below.

To understand the results of mobility, we calculated the mean free path $l_e$ of the electrons as a function of temperature, as shown in Fig. 6(b). The mean free path can be calculated with the following formula:

$$l_e = \sqrt{2E_F m^*}\frac{\mu}{e}. \quad (1)$$

Here, $E_F$ is the Fermi energy and $e$ is the elemental charge. The Fermi energy was computed from the reduced electron chemical potential $\eta = E_F/k_B T$ with the Boltzmann constant $k_B$. The reduced electron chemical potential $\eta$ was calculated after Nilsson.[25] This method interpolates the range between non-degenerated and degenerated semiconductors and determines the reduced electron chemical potential $\eta$ as follows:

$$\eta = \frac{\ln\frac{n}{N_C}}{1-\left(\frac{n}{N_C}\right)^2} + \nu\left(1 - \frac{1}{1+(0.24+1.08\nu)^2}\right), \quad (2)$$

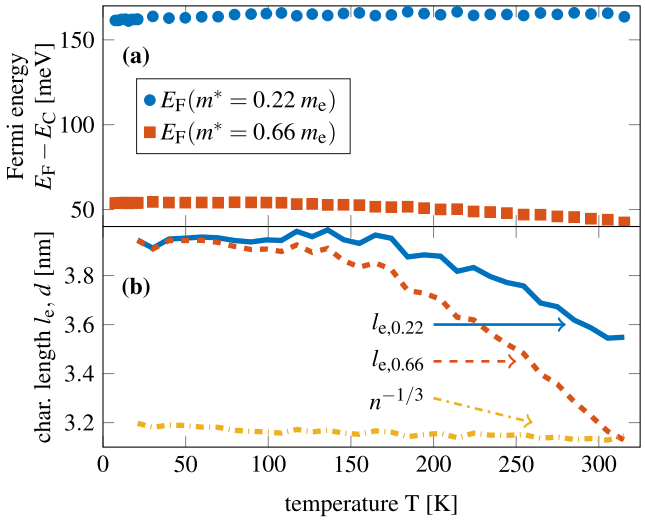


**FIG. 6**. (a) Calculated [Eq. (2)] relative Fermi energy for effective masses of $m^* = 0.22m_e$ (blue dots) and $m^* = 0.66m_e$ (red squares) as a function of temperature is shown. The Fermi level lies in the conduction band at all temperatures and shows only weak temperature dependence and (b) the calculated mean free path [Eq. (1)] $l_{e,m^*/m_e}$ of the electrons as a function of temperature $T$ for $m^* = 0.22m_e$ (blue solid line) and $m^* = 0.66m_e$ (red dashed line), as well as the mean free distance between single ionized donors $n^{-1/3}$ (yellow dashed dotted line), assuming a simple cubic distribution, is shown.

$$v = \left(\frac{3\sqrt{\pi}\frac{n}{N_C}}{4}\right)^{2/3}, \tag{3}$$

with $N_C$ being the effective density of states in the conduction band,

$$N_C = 2\left(\frac{2\pi m^* k_B T}{h^2}\right)^{3/2}, \tag{4}$$

with $h$ being the Planck constant. For effective masses of $m^* = 0.22m_e$ and $m^* = 0.66m_e$, Fermi energies of 160 meV and 50 meV, respectively, above the conduction band minimum were obtained. This can be seen in Fig. 6(a). Even though Eq. (2) is valid for non-degenerate and degenerate semiconductors, the results shown in Fig. 6 give only a rough estimation since the effective mass model does not consider the occupation of the conduction band.

In order to determine the thermoelectric properties, the thermovoltage is measured as a function of temperature difference. Figure 7 shows the normalized thermovoltage as a function of normalized temperature difference for bath temperatures of 30 K, 100 K, and 295 K. Small offsets ($U_{os} < 50\,\mu$V) have been subtracted from the data. The Seebeck coefficient is determined by

$$S = -\frac{U_{th}}{\Delta T}. \tag{5}$$

The change in the Seebeck coefficient as a function of bath temperature can be observed by the change in the slope of linear fits. Furthermore, the maximum achieved temperature difference $\Delta T_{max}$ is depicted in Fig. 7.

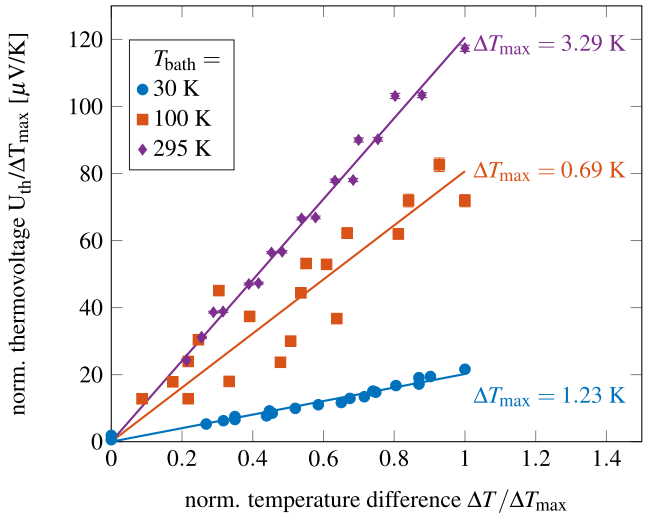


**FIG. 7**. Measured thermovoltage $U_{th}$ normalized by the maximum of the temperature difference at different bath temperatures as a function of the normalized temperature difference. An offset $U_{os} < 50\,\mu$V has been subtracted from the plotted data.

The Seebeck coefficient $S$ has been determined for temperatures between 30 K and 320 K. The results are shown in Fig. 8 as a function of temperature $T$. The Seebeck coefficients are in the range of $S = -25\,\mu$V/K at $T = 30$ K to $S = -125\,\mu$V/K at room temperature.

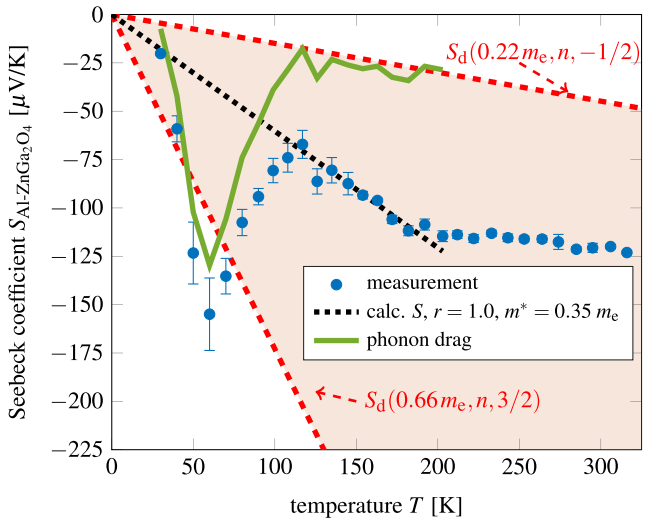


**FIG. 8**. Seebeck coefficient $S$ as a function of temperature $T$. The red area marks the values for the Seebeck coefficients, which can be calculated with Eq. (11) if the effective mass and scattering parameter are varied between 0.22–0.66$m_e$ and −1/2 to 3/2, respectively. For $T \leq 200$ K, a calculated Seebeck coefficient with $r = 1.0$ and $m^* = 0.35m_e$ has been plotted (black dotted line), which fits the data well for 100 K $\leq T \leq$ 200 K. Furthermore, for $T \leq 200$ K, the difference between the measured and calculated Seebeck coefficients has been plotted and is assumed to be due to the phonon drag effect (green solid line).

Below room temperature, the magnitude of the Seebeck coefficient decreases steadily down to $T = 100$ K. For lower temperatures, it shows a maximum at $T = 60$ K.

## IV. DISCUSSION

We discuss all electrical and thermoelectrical properties in detail. The electrical conductivity, as shown in Fig. 3, has a weak temperature dependence when compared with that of $\beta$-$Ga_2O_3$.[23] The qualitative temperature dependence is as expected for semiconductors. Below room temperature, the conductivity increases due to the decrease in electron–phonon interaction and decreases when defect scattering becomes more dominant. From a quantitative perspective, the weak temperature dependence originates partly from the very weak temperature dependence of the Hall charge carrier density, as shown in Fig. 4. The unintentionally doped $ZnGa_2O_4$ is a degenerate semiconductor, which we conclude from the high magnitude and the weak temperature dependence of the charge carrier density and the calculated relative Fermi level shown in Fig. 6(a), which is above the lower conduction band edge for all cases. Furthermore, this is in agreement with the Mott criterion, which gives an approximation for a critical charge carrier density $n_c = \left(\frac{m^* e^2}{16\pi\varepsilon_0\varepsilon_s\hbar^2}\right)^3$ above which the semiconductor is degenerate. $\varepsilon_0$ is the vacuum permittivity, and $\hbar$ is the reduced Planck's constant. For the static dielectric constant, $\varepsilon_s = 9.88$ has been used, which was obtained for $Zn_{0.99}Cu_{0.01}Ga_2O_4$.[26] The critical charge carrier density is $n_c(m^* = 0.22 \cdot m_e) = 1.2 \times 10^{18}$ cm$^{-3}$ and $n_c(m^* = 0.66 \cdot m_e) = 3.1 \times 10^{19}$ cm$^{-3}$, depending on the assumed effective masses $m^* = 0.22$–$0.66 m_e$. The critical carrier density lies underneath the Hall charge carrier density for all cases. At present, the origin of the charge carriers remains unknown. However, theoretical studies have calculated formation energies of various defects in $ZnGa_2O_4$, like nitrogen.[16,38] One could think of native defects, such as antisite defects of Ga and Zn or oxygen vacancies. On the other hand, impurities within the crystal could lead to electrical conductivity as well. Due to the position of the relative Fermi level, conduction within the conduction band is expected to be the major charge transport mechanism, and only weak contributions of impurity bands, as observed in $\beta$-$Ga_2O_3$,[39] are assumed and therefore neglected.

The charge carrier mobility was calculated and is shown in Fig. 5. The room temperature value is lower than the best value reported[9] but is within the range of reported values. This indicates that there are a higher number of defects in the sample investigated. For the high temperature regime, the mobility is limited by optical phonon (OP) scattering. OP scattering can deviate significantly from the $T^{-3/2}$ dependence of acoustic deformation potential scattering[27] due to its inelastic nature.

In chemically related TCOs $\beta$-$Ga_2O_3$[28] and ZnO,[29] it was shown that polar optical phonon scattering is the dominant scattering mechanism at high temperatures due to partial ionic bonding. The following equation by Askerov has proved to be useful for the interpretation of polar optical phonon scattering in degenerate ZnO films:[29,30]

$$\mu_{\mathrm{POP,deg}} = \frac{e\hbar}{4\alpha E_{\mathrm{POP}} m^*}\left(e^{\frac{E_{\mathrm{POP}}}{k_B T}} + 1\right), \tag{6}$$

with

$$\alpha = \left(\frac{1}{\varepsilon_\infty} - \frac{1}{\varepsilon_s}\right)\frac{\sqrt{m^*}e^2}{4\pi\varepsilon_0\hbar\sqrt{2E_{\mathrm{POP}}}}. \tag{7}$$

Here, $E_{\mathrm{POP}}$ is the average energy of the optical phonons, $\alpha$ is the polar coupling constant, and $\varepsilon_\infty$ is the high frequency dielectric constant. The high frequency dielectric constant of $\beta$-$Ga_2O_3$[31,32] ($\varepsilon_\infty = 3.57$) has been used since the exact value for $ZnGa_2O_4$ is unknown, and it is expected in the same range as the values for ZnO[33,34] ($\varepsilon_\infty \approx 3.7$).

The mean free path in Fig. 6(b) shows that there is a temperature independent process that limits the mean free path at $l_{e,max} = 4$ nm. This limit becomes clear for temperatures lower than $T \leq 180$ K when the electron–phonon interaction becomes weaker. Furthermore, the mean free distance between single ionized donors, assuming a simple cubic distribution, is shown. This simple model is justified since the base lattice formed by the $O^{2-}$ ions is a cubic crystal system. One can see that there is an upper limit of $l_{e,max} = 4$ nm and that the simple model for the donor distribution predicts a mean distance in the same range.

There are two approaches to explain the low temperature limit of the electron mobility. On the one hand, it can be explained by the scattering of electrons with neutral impurities. The Hall charge carrier data shown in Fig. 4 suggests a constant ionization of the donors, acceptors, and vacancies for the investigated temperature interval; hence, $N_{\mathrm{II}} = const$. This leads to the assumption that the neutral impurity density $N_{\mathrm{NI}} = const$ as well. Electron scattering on neutral impurities can be described by[27] $\mu_{\mathrm{NI}} \propto N_{\mathrm{NI}}^{-1}$. Thus, if there is no change in concentration of the neutral impurities, there will be a temperature independent upper limit of the mobility, which can be observed in Fig. 5.

On the other hand, high electron concentrations in semiconductors mean that there is either a high concentration of singly ionized impurities or a lower density of ionized impurities with a higher degree of ionization. Furthermore, the scattering of electrons in degenerate semiconductors with ionized impurities can be described by the Brooks–Herring equation,[35] which has been successfully applied to degenerate ZnO films[29,36] and has a weak temperature dependence,

$$\mu_{\mathrm{II,deg}} = \frac{n}{Z^2 N_{\mathrm{II}}}\frac{24\pi^3(\varepsilon_0\varepsilon_s)^2\hbar^3}{e^3 m^{*2}}\frac{1}{\ln[1+\beta(n)] - \frac{\beta(n)}{1+\beta(n)}}, \tag{8}$$

with

$$\beta(n) = \frac{3^{1/3}4\pi^{8/3}\varepsilon_0\varepsilon_s\hbar^2 n^{1/3}}{e^2 m^*}. \tag{9}$$

Here, $Z$ is the degree of ionization, and $N_{\mathrm{II}} = N_{\mathrm{D}} + N_{\mathrm{A}} = 2N_{\mathrm{A}} + n$ is the density of ionized impurities, with donator and acceptor densities $N_{\mathrm{D}}$ and $N_{\mathrm{A}}$, respectively. Ionized impurity scattering is expected to be more dominant since there is a high density of ionized donors due to the high Hall charge carrier density.

The fits shown in Fig. 5 have been calculated using Matthiessen's rule; considering the scattering on polar optical phonons and ionized impurities after Eqs. (6) and (8), respectively, we get

$$\mu = \left(\frac{1}{\mu_{\mathrm{POP,deg}}} + \frac{1}{\mu_{\mathrm{II,deg}}}\right)^{-1}, \tag{10}$$

for effective masses of $m^* = 0.22m_e$ and $m^* = 0.66m_e$. The $m^* = 0.22m_e$ fit (red dashed line) results in an acceptor density $N_A = 6.65 \times 10^{19}$ cm$^{-3}$ and a phonon energy $E_{POP} = 87$ meV. For the $m^* = 0.66m_e$ fit (yellow dotted line), an acceptor density $N_A = 6.15 \times 10^{18}$ cm$^{-3}$ and a phonon energy $E_{POP} = 140$ meV were obtained. These results lead to compensation ratios ($N_A/N_D$) between 13% and 70% for $m^* = 0.66m_e$ and $m^* = 0.22m_e$, respectively. The fit results reported are to be understood as an estimation of the experimentally obtained acceptor density, donor density, and phonon energy and may be used to compare the intrinsic properties with those of other degenerate TCOs, where the same fit models may be applied. The high compensation ratios are due to the high donator and acceptor densities, which could originate from a high amount of $Zn^{2+}/Ga^{3+}$ antisite defects. The high charge carrier density could be caused by electrically active antisite defects as well as oxygen vacancies. The origin of ionized impurities needs further investigation.

The measurement of thermovoltage as a function of temperature difference, as shown in Fig. 7, reveals that there is a major change in the maximum reached temperature difference for different bath temperatures. This also correlates with the precision of the data points. The maximum reached temperature difference depends on the imprinted heating power but is more strongly dependent on the thermal conductivity of the material. The higher the thermal conductivity of the material, the more difficult it is to create large temperature differences. This is the main reason for the increasing uncertainty of the Seebeck coefficient at lower bath temperatures. From the change of maximum temperature difference, one can conclude the change of the thermal conductivity of the material. Having a look at the error bars of the Seebeck coefficient in Fig. 8, which is correlated with the maximum temperature difference and, therefore, with the thermal conductivity, one can see that the thermal conductivity seems to have a maximum value around $T_{bath} = 60$ K and decreases as the temperature decreases further. This could be due to a distortion of the lattice, which has been reported in Ref. 9 as particles revealing Moiré patterns in transmission electron microscopy bright field images.

The Seebeck coefficient (Fig. 8) is negative, which means that electrons are the major charge carriers. This is in agreement with the Hall charge carrier results. The Seebeck coefficient is lower than the one reported[24] for $\beta$-$Ga_2O_3$ in the same temperature regime. This can be understood since the semiconducting oxide investigated here is degenerate.

The red area in Fig. 8 marks the calculated Seebeck coefficients following the commonly used equation[27,40] for degenerate semiconductors, assuming the effective mass to be between $m^* = 0.22m_e$ and $m^* = 0.66m_e$ and the scattering factor $r$ to be between $r = -0.5$ and $r = 1.5$,

$$S_d(m^*, n, r) = -\frac{k_B}{e}\left(r + \frac{3}{2}\right)\frac{\pi^2}{3}\frac{1}{\eta}. \quad (11)$$

The scattering parameter $r$ is based on the assumption that the electron relaxation time $\tau_e$ follows a power law dependence $\tau_e \propto E^r$. In other investigations, it was observed that $\mu \propto E^{r'}$ and $r \cong r' + 1$ hold well in the investigated temperature interval. In general, $\mu = \mu(E, T)$ and $r'$ are calculated by the assumption $E = E(T) = k_B T$ and

$$\frac{d\ln(\mu)}{d\ln(T)} = r' + \frac{\partial r}{\partial \ln(T)}. \quad (12)$$

A calculated Seebeck coefficient with $r = 1.0$ and $m^* = 0.35m_e$ was added as a thin black dashed line, which fits the data for 100 K $\leq T \leq$ 200 K best. For $T < 200$ K, the difference in the calculated Seebeck coefficient with $r = 1.0$, $m^* = 0.35m_e$, and the measured Seebeck coefficient is plotted as a green solid line. We conclude that the observed deviation in the theoretical Seebeck coefficient is due to the phonon drag (PD) effect,[41,42] which has a maximum value of about $S_{PD} \approx 125$ $\mu$V/K at $T = 60$ K. A more quantitative analysis of the phonon drag effect requires detailed knowledge of the scattering parameter and therefore a deeper understanding of the scattering mechanisms limiting the charge transport in $ZnGa_2O_4$.

## V. CONCLUSION

In conclusion, we have shown that as-grown bulk $ZnGa_2O_4$ single crystals show a higher electrical conductivity at room temperature ($\sigma_{ZnGa_2O_4} \approx 300$ S/cm) than that shown in earlier investigated $ZnGa_2O_4$ ceramics ($\sigma_{ZnGa_2O_{4,ceram.}} \approx 30$ S/cm[19]), as-grown $\beta$-$Ga_2O_3$ bulk ($\sigma_{\beta-Ga_2O_3} \approx 3$ S/cm[23]), or as-grown ZnO bulk ($\sigma_{ZnO} \approx 40$ S/cm[37]) due to the high charge carrier density. The donor mechanisms remain to be established. The wide bandgap of the material makes it suitable for application in high-power devices, which can become even more promising if $p$-doped material becomes available. In terms of the power factor $Pf = \sigma S^2$ for thermoelectric applications, $ZnGa_2O_4$ has a room temperature value of $Pf_{ZnGa_2O_4} \approx 4.7$ $\mu$W/K, which is more than 5 times higher than that of $\beta$-$Ga_2O_3$, with $Pf_{\beta-Ga_2O_3} \approx 0.8$ $\mu$W/K. Therefore, $ZnGa_2O_4$ is a more promising material for thermoelectric applications of transparent conducting oxides.

## ACKNOWLEDGMENTS

This work was performed in the framework of GraFOx, a Leibniz-ScienceCampus partially funded by the Leibniz association and by the German Science Foundation (Grant Nos. DFG-FI932/10-1 and DFG-FI932/11-1).

## DATA AVAILABILITY

The data that support the findings of this study are available within the article.

## REFERENCES

[1] M. Grundmann, H. Frenzel, A. Lajn, M. Lorenz, F. Schein, and H. von Wenckstern, "Transparent semiconducting oxides: Materials and devices," Phys. Status Solidi A **207**, 1437–1449 (2010).

[2] M. Lorenz, M. S. R. Rao, T. Venkatesan, E. Fortunato, P. Barquinha, R. Branquinho, D. Salgueiro, R. Martins, E. Carlos, A. Liu, F. K. Shan, M. Grundmann, H. Boschker, J. Mukherjee, M. Priyadarshini, N. DasGupta, D. J. Rogers, F. H. Teherani, E. V. Sandana, P. Bove, K. Rietwyk, A. Zaban, A. Veziridis, A. Weidenkaff, M. Muralidhar, M. Murakami, S. Abel, J. Fompeyrine, J. Zuniga-Perez, R. Ramesh, N. A. Spaldin, S. Ostanin, V. Borisov, I. Mertig, V. Lazenka, G. Srinivasan, W. Prellier, M. Uchida, M. Kawasaki, R. Pentcheva, P. Gegenwart, F. M. Granozio, J. Fontcuberta, and N. Pryds, "The 2016 oxide electronic materials and oxide interfaces roadmap," J. Phys. D: Appl. Phys. **49**, 433001 (2016).

[3] E. Fortunato, P. Barquinha, and R. Martins, "Oxide semiconductor thin-film transistors: A review of recent advances," Adv. Mater. **24**, 2945–2986 (2012).

[4]M. Higashiwaki, H. Murakami, Y. Kumagai, and A. Kuramata, "Current status of $Ga_2O_3$ power devices," Jpn. J. Appl. Phys., Part 1 **55**, 1202A1 (2016).
[5]N. Suzuki, S. Ohira, M. Tanaka, T. Sugawara, K. Nakajima, and T. Shishido, "Fabrication and characterization of transparent conductive Sn-doped $\beta$-$Ga_2O_3$ single crystal," Phys. Status Solidi C **4**, 2310–2313 (2007).
[6]A. J. Green, K. D. Chabak, E. R. Heller, R. C. Fitch, M. Baldini, A. Fiedler, K. Irmscher, G. Wagner, Z. Galazka, S. E. Tetlak, A. Crespo, K. Leedy, and G. H. Jessen, "3.8-MV/cm breakdown strength of MOVPE-grown Sn-doped-$Ga_2O_3$ mosfets," IEEE Electron Device Lett. **37**, 902–905 (2016).
[7]K. D. Chabak, N. Moser, A. J. Green, D. E. Walker, S. E. Tetlak, E. Heller, A. Crespo, R. Fitch, J. P. McCandless, K. Leedy, M. Baldini, G. Wagner, Z. Galazka, X. Li, and G. Jessen, "Enhancement-mode $Ga_2O_3$ wrap-gate fin field-effect transistors on native (100) $\beta$-$Ga_2O_3$ substrate with high breakdown voltage," Appl. Phys. Lett. **109**, 213501 (2016).
[8]Z. Galazka, "$\beta$-$Ga_2O_3$ for wide-bandgap electronics and optoelectronics," Semicond. Sci. Technol. **33**, 113001 (2018).
[9]Z. Galazka, S. Ganschow, R. Schewski, K. Irmscher, D. Klimm, A. Kwasniewski, M. Pietsch, A. Fiedler, I. Schulze-Jonack, M. Albrecht, T. Schröder, and M. Bickermann, "Ultra-wide bandgap, conductive, high mobility, and high quality melt-grown bulk $ZnGa_2O_4$ single crystals," APL Mater. **7**, 022512 (2019).
[10]F. Zerarga, A. Bouhemadou, R. Khenata, and S. Bin-Omran, "Structural, electronic and optical properties of spinel oxides $ZnAl_2O_4$, $ZnGa_2O_4$ and $ZnIn_2O_4$," Solid State Sci. **13**, 1638–1648 (2011).
[11]L. Pisani, T. Maitra, and R. Valentí, "Effects of Fe substitution on the electronic, transport, and magnetic properties of $ZnGa_2O_4$: A systematic *ab initio* study," Phys. Rev. B **73**, 205204 (2006).
[12]S. López, A. H. Romero, P. Rodríguez-Hernández, and A. Muñoz, "First-principles study of the high-pressure phase transition in $ZnAl_2O_4$ and $ZnGa_2O_4$: From cubic spinel to orthorhombic post-spinel structures," Phys. Rev. B **79**, 214103 (2009).
[13]S. Z. Karazhanov and P. Ravindran, "*Ab initio* study of double oxides $ZnX_2O_4$ (X = Al, Ga, In) having spinel structure," J. Am. Ceram. Soc. **93**, 3335–3341 (2010).
[14]M. G. Brik, "First-principles calculations of electronic, optical and elastic properties of $ZnAl_2S_4$ and $ZnGa_2O_4$," J. Phys. Chem. Solids **71**, 1435–1442 (2010).
[15]H. Dixit, N. Tandon, S. Cottenier, R. Saniz, D. Lamoen, B. Partoens, V. Van Speybroeck, and M. Waroquier, "Electronic structure and band gap of zinc spinel oxides beyond LDA: $ZnAl_2O_4$, $ZnGa_2O_4$ and $ZnIn_2O_4$," New J. Phys. **13**, 063002 (2011).
[16]Y. Xia, T. Wang, X. Zhao, X. Jiao, and D. Chen, "Theoretical and experimental investigations on effects of native point defects and nitrogen doping on the optical band structure of spinel $ZnGa_2O_4$," J. Phys. Chem. C **122**, 5509–5517 (2018).
[17]S. K. Sampath, D. G. Kanhere, and R. Pandey, "Electronic structure of spinel oxides: Zinc aluminate and zinc gallate," J. Phys.: Condens. Matter **11**, 3635–3644 (1999).
[18]S. K. Sampath and J. F. Cordaro, "Optical properties of zinc aluminate, zinc gallate, and zinc aluminogallate spinels," J. Am. Ceram. Soc. **81**, 649–654 (2005).
[19]T. Omata, N. Ueda, K. Ueda, and H. Kawazoe, "New ultraviolet-transport electroconductive oxide, $ZnGa_2O_4$ spinel," Appl. Phys. Lett. **64**, 1077–1078 (1994).
[20]T. Oshima, M. Niwa, A. Mukai, T. Nagami, T. Suyama, and A. Ohtomo, "Epitaxial growth of wide-band-gap $ZnGa_2O_4$ films by mist chemical vapor deposition," J. Cryst. Growth **386**, 190–193 (2014).
[21]W. Zhang, J. Zhang, Y. Li, Z. Chen, and T. Wang, "Preparation and optical properties of $ZnGa_2O_4$:$Cr^{3+}$ thin films derived by sol-gel process," Appl. Surf. Sci. **256**, 4702–4707 (2010).
[22]Z. Yan, H. Takei, and H. Kawazoe, "Electrical conductivity in transparent $ZnGa_2O_4$: Reduction and surface-layer structure transformation," J. Am. Ceram. Soc. **81**, 180–186 (2005).
[23]R. Ahrling, J. Boy, M. Handwerg, O. Chiatti, R. Mitdank, G. Wagner, Z. Galazka, and S. F. Fischer, "Transport properties and finite size effects in $\beta$-$Ga_2O_3$ thin films," Sci. Rep. **9**, 13149 (2019).
[24]J. Boy, M. Handwerg, R. Ahrling, R. Mitdank, G. Wagner, Z. Galazka, and S. F. Fischer, "Temperature dependence of the Seebeck coefficient of epitaxial $\beta$-$Ga_2O_3$ thin films," APL Mater. **7**, 022526 (2019).
[25]N. G. Nilsson, "An accurate approximation of the generalized Einstein relation for degenerate semiconductors," Phys. Status Solidi A **19**, K75 (1973).
[26]X. Lu, W. Bian, Y. Li, H. Zhu, Z. Fu, and Q. Zhang, "Cation distributions and microwave dielectric properties of Cu-substituted $ZnGa_2O_4$ spinel ceramics," Ceram. Int. **43**, 13839–13844 (2017).
[27]K. Seeger, in *Semiconductor Physics*, 9th ed., edited by H. von Riedesel (Springer, 2004).
[28]N. Ma, N. Tanen, A. Verma, Z. Guo, T. Luo, H. G. Xing, and D. Jena, "Intrinsic electron mobility limits in $\beta$-$Ga_2O_3$," Appl. Phys. Lett. **109**, 212101 (2016).
[29]A. Bikowski and K. Ellmer, "Analytical model of electron transport in polycrystalline, degenerately doped ZnO films," J. Appl. Phys. **116**, 143704 (2014).
[30]B. M. Askerov, *Electron Transport Phenomena in Semiconductors* (World Scientific, 1994).
[31]M. Passlack, N. E. J. Hunt, E. F. Schubert, G. J. Zydzik, M. Hong, J. P. Mannaerts, R. L. Opila, and R. J. Fischer, "Dielectric properties of electron-beam deposited $Ga_2O_3$ films," Appl. Phys. Lett. **64**, 2715–2717 (1994).
[32]M. Rebien, W. Henrion, M. Hong, J. P. Mannaerts, and M. Fleischer, "Optical properties of gallium oxide thin films," Appl. Phys. Lett. **81**, 250–252 (2002).
[33]N. Ashkenov, B. N. Mbenkum, C. Bundesmann, V. Riede, M. Lorenz, D. Spemann, E. M. Kaidashev, A. Kasic, M. Schubert, M. Grundmann, G. Wagner, H. Neumann, V. Darakchieva, H. Arwin, and B. Monemar, "Infrared dielectric functions and phonon modes of high-quality ZnO films," J. Appl. Phys. **93**, 126–133 (2003).
[34]F. Decremps, J. Pellicer-Porres, A. M. Saitta, J.-C. Chervin, and A. Polian, "High-pressure Raman spectroscopy study of wurtzite ZnO," Phys. Rev. B **65**, 092101 (2002).
[35]R. Dingle, "XCIV. Scattering of electrons and holes by charged donors and acceptors in semiconductors," London, Edinburgh, Dublin Philos. Mag. J. Sci. **46**, 831–840 (1955).
[36]K. Ellmer, "Resistivity of polycrystalline zinc oxide films: Current status and physical limit," J. Phys. D: Appl. Phys. **34**, 3097–3108 (2001).
[37]L. Xin-Hua, X. Jia-Yue, J. Min, S. Hui, and L. Xiao-Min, "Electrical and optical properties of bulk ZnO single crystal grown by flux Bridgman method," Chin. Phys. Lett. **23**, 3356–3358 (2006).
[38]P. Li, X. Zhao, H. Sun, L. Wang, B. Song, B. Gao, and W. Fan, "Theoretical studies on the form and effect of n-doping in an $ZnGa_2O_4$ photocatalyst," RSC Adv. **6**, 74483–74492 (2016).
[39]Z. Kabilova, C. Kurdak, and R. L. Peterson, "Observation of impurity band conduction and variable range hopping in heavily doped (010) $\beta$-$Ga_2O_3$," Semicond. Sci. Technol. **34**, 03LT02 (2019).
[40]N. Preissler, O. Bierwagen, A. T. Ramu, and J. S. Speck, "Electrical transport, electrothermal transport, and effective electron mass in single-crystalline $In_2O_3$ films," Phys. Rev. B **88**, 085305 (2013).
[41]G. D. Mahan, L. Lindsay, and D. A. Broido, "The Seebeck coefficient and phonon drag in silicon," J. Appl. Phys. **116**, 245102 (2014).
[42]M. Kockert, D. Kojda, R. Mitdank, A. Mogilatenko, Z. Wang, J. Ruhhammer, M. Kroener, P. Woias, and S. F. Fischer, "Nanometrology: Absolute Seebeck coefficient of individual silver nanowires," Sci. Rep. **9**, 20265 (2019).